Giorgio Besagni[1]
Department of Energy,
Politecnico di Milano,
Via Lambruschini 4,
Milan 20156, Italy
e-mail: giorgio.besagni@polimi.it

Gaël Raymond Guédon
Department of Energy,
Politecnico di Milano,
Via Lambruschini 4,
Milan 20156, Italy
e-mail: gaelraymond.guedon@polimi.it

Fabio Inzoli
Department of Energy,
Politecnico di Milano,
Via Lambruschini 4,
Milan 20156, Italy
e-mail: fabio.inzoli@polimi.it

Annular Gap Bubble Column: Experimental Investigation and Computational Fluid Dynamics Modeling

This paper investigates the countercurrent gas–liquid flow in an annular gap bubble column with a 0.24 m inner diameter by using experimental and numerical investigations. The two-phase flow is studied experimentally using flow visualizations, gas holdup measurements, and double fiber optical probes in the following range of operating conditions: superficial air velocities up to 0.23 m/s and superficial water velocities up to −0.11 m/s, corresponding to gas holdups up to 29%. The flow visualizations were used to observe the flow patterns and to obtain the bubble size distribution (BSD). The gas holdup measurements were used for investigating the flow regime transitions, and the double fiber optical probes were used to study the local flow phenomena. A computational fluid dynamics (CFD) Eulerian two-fluid modeling of the column operating in the bubbly flow regime is proposed using the commercial software ANSYS FLUENT*. The three-dimensional (3D) transient simulations have been performed considering a set of nondrag forces and polydispersity. It is shown that the errors in the global holdup and in the local properties are below 7% and 16%, respectively, in the range considered.* [DOI: 10.1115/1.4031002]

1 Introduction

Gas–liquid flow in vertical pipes and bubble columns is encountered in several plants in the chemical, energy, and nuclear fields. The correct design and operation of these devices can be managed with the proper prediction of the flow patterns and properties. This study investigates the countercurrent air–water flow in a large-diameter vertical pipe with internal pipes ("countercurrent annular bubble column"). This study considers a pipe with an inner diameter of 0.24 m, which is a large-diameter pipe under ambient operating conditions.

The size range of a pipe is determined by the dimensionless diameter D_H^*

$$D_H^* = \frac{D_H}{\sqrt{\sigma/g(\rho_L - \rho_G)}} \tag{1}$$

where D_H is the hydraulic diameter, σ is the surface tension coefficient, g is the gravity acceleration, and $\rho_L - \rho_G$ is the density difference between the two phases. Pipes with dimensionless diameters greater than the critical value $D_{H,\mathrm{cr}}^* = 52$ are considered large-diameter pipes [1]. The critical hydraulic diameter for air–water at atmospheric conditions is $D_{H,\mathrm{cr}} \approx 0.13$ m. When the pipe diameter is larger than this value, the stabilizing effect of the channel wall on the interface of the Taylor bubbles becomes lower, and the slug flow can no longer be sustained due to the Rayleigh–Taylor instabilities. The hydrodynamics in large pipes differ from those in small pipes because of changes in the liquid field around the bubbles, the presence of additional turbulence, and strong secondary recirculation [2]. Therefore, the flow regime maps and flow regime transitions criteria used to predict the behavior of two-phase flow in small pipes may not be scaled up for understanding the flow in large ones.

This study considers countercurrent gas–liquid vertical flow. Countercurrent two-phase flow has been investigated experimentally using intrusive and nonintrusive techniques. Yamaguchi and Yamazaki [3] investigated cross-sectional void fractions of cocurrent and countercurrent bubbly and slug air–water flow in vertical pipes with inner diameters of 0.04 and 0.08 m ($D_H^* = 14.69$–29.38) by a quick-closing valve method. Hasan et al. [4] investigated cross-sectional void fractions of air–water cocurrent and countercurrent bubbly and slug flow in a vertical pipe with an inner diameter of 0.127 m ($D_H^* = 46.64$) using a pressure drop technique. Aritomi et al. [5] investigated the behaviors of countercurrent bubbly flow in a rectangular channel ($D_H^* = 18.18$) using an ultrasonic technique. Fuangworawong et al. [6] investigated local void fractions of air–water countercurrent bubbly flow in a vertical pipe with an inner diameter of 0.050 m ($D_H^* = 18.18$) using a wire mesh tomography technique. Ghosh et al. [7,8] investigated cross-sectional void fractions of air–water countercurrent flow in a vertical pipe with an inner diameter of 0.0264 m ($D_H^* = 9.69$) using a wire conductivity probe technique. All of these studies evaluated the fluid dynamics behavior with a dimensionless diameter smaller than the critical value of 52. The facility studied in this paper has an inner diameter of 0.24 m, corresponding to a dimensionless diameter of $D_H^* = 88.13$ (above the critical value), without considering the internal pipes, and $D_H^* = 47.37$ in the annular gap configuration (close to the critical value).

Previous studies have focused on open tubes (without inner pipes), but many chemical and nuclear engineering systems involve more complex geometries in separators, fuel bundles, and steam generators. Annular channels have been found to replicate some of the phenomena found in these more complex geometries. Annular channels also occur in internal-loop, airlift bubble columns and photocatalytic bubble column reactors containing lamps positioned on the centerline [9]. However, in the literature, the studies focused on annular channel configurations typically concern null superficial water velocity or cocurrent flow in a small-diameter pipe [10–12]. The countercurrent flow in large-diameter pipes with annular gap is not yet well understood. The first experimental results of the present configuration have been proposed [13], but some open questions remain, such as the flow regime

[1]Corresponding author.

Contributed by the Fluids Engineering Division of ASME for publication in the JOURNAL OF FLUIDS ENGINEERING. Manuscript received February 24, 2015; final manuscript received June 26, 2015; published online August 10, 2015. Assoc. Editor: Riccardo Mereu.

transitions, the bubble diameter distribution, and the numerical settings for the modeling of the facility.

The ability to predict the fluid dynamics is of primary importance in designing and developing multiphase reactors. Numerical modeling of multiphase flows at large scales is an intensive area of research, and the Eulerian two-fluid approach is widely used for simulating dispersed multiphase flows, such as in bubble columns. In this approach, the conservation equations are formulated for each phase and weighted with the volume fraction of the corresponding phase. As a result of this averaging procedure, the interaction between the phases is taken into account by the interfacial exchange terms that appear in the mass, momentum, and energy conservation equations of each phase. The turbulence for large-scale simulations is usually described with the Reynolds-Averaged Navier–Stokes (RANS) equations [14]. Such an approach allows for the simulation of large-scale reactors, whereas direct numerical simulation or large eddy simulation with the Euler–Lagrange treatment is too cost-intensive.

Examples of the Eulerian two-fluid approach with unsteady RANS (URANS) turbulence modeling have been widely applied in the literature for bubble columns [14–20]. When using an Eulerian two-fluid approach, a proper solution for the bubble columns is dependent on the correct modeling of interphase forces and turbulence models. These closure models must describe complex phase interactions, and several models for interphase forces have been reported in the literature [15,19,21–23]. The drag force has a great effect on the macroscopic flow patterns (i.e., vertical velocity profiles and local void fraction profiles). The lateral forces influence the radial void fractions in the pipe cross section. The lift force is subject to a change of sign for a bubble critical diameter and becomes substantial by using bubble classes with extra velocity classes. The wall force drives the bubbles away from the wall, and the turbulent dispersion force tends to even the gradients in the void fractions.

In this paper, the two-phase flow is studied using experimental and numerical investigations. The two-phase flow is studied experimentally using flow visualizations, gas holdup measurements, and double fiber optical probes in the following range of operating conditions: superficial air velocities up to 0.23 m/s and superficial water velocities up to −0.11 m/s, corresponding to gas holdups up to 29%. The flow visualizations were used to observe the flow patterns and to obtain the bubble size distribution (BSD). The gas holdup measurements were used to investigate the flow regime transitions, and the double fiber optical probes were used to study the local flow phenomena. The numerical part concerns numerical calculations performed with an Eulerian two-fluid model, using the commercial software ANSYS FLUENT Release 15.0.7. The 3D transient simulations considered a set of nondrag forces (drag, lift, wall force, and turbulent dispersion) and polydispersity within an Eulerian two-fluid approach. It is shown that the errors in the global holdup and in the local properties are below 7% and 16%, respectively, in the range considered.

The paper is structured as follows: In Sec. 2, the experimental setup is presented. In Sec. 3, the numerical approach is presented. In Sec. 4, the experimental results are detailed and in Sec. 5, numerical prediction is compared with the experiments. Finally, in Sec. 6, the results are discussed, and conclusions are drawn.

2 The Experimental Setup

2.1 Experimental Facility. The experimental facility (Figs.1(*a*)–1(*c*)) is a nonpressurized vertical pipe made of Plexiglas with $d_{inner} = 0.24$ m and $H_{column} = 5.3$ m. Two internal pipes made of polyvinyl chloride are positioned: one centrally positioned (with an external diameter of 0.06 m) and one asymmetrically positioned (with an external diameter of 0.075 m). A pump, controlled by a bypass valve, provides water recirculation, and a rotameter (3) measures the water flow rate. The recirculated water falls down on the water surface from the top of the column. A pressure reducer controls the pressure upstream from rotameters (1) and (2) and is used to measure the airflow rate. The air distributor, which is positioned asymmetrically (on the lateral inner pipe), is made of a stainless steel tube with an external diameter of 0.07 m, a height of 0.34 m, and holes positioned along the circumference with diameters $d_{holes} = 3.5$ mm (Fig. 1(*b*)). The optical probe is inserted, via an access port (Fig. 2), into the flow 2.3 m from the pipe bottom (1.9 m from the air distributor). Clean filtered deionized water was used. During the experiments, the air and water temperatures were controlled to maintain constant values.

In this study, the values of gas density (used to compute the superficial gas velocity) are based upon the operating conditions existing at the column midpoint [24]. The midpoint column pressure was assumed equal to the column outlet pressure plus one-half the total experimental hydrostatic pressure head.

2.2 Measurement Techniques. Digital images were taken to have detailed descriptions regarding bubble shapes and flow configurations and qualitative information on fluid dynamics. The holdup measurements were determined using the bed expansion technique. The local bubble properties were measured using a double fiber optical probe. In Secs. 2.2.1, 2.2.2, and 2.2.3, the measurement techniques are detailed.

2.2.1 Digital Images and Image Processing

2.2.1.1 Instrumentation. Photos were taken using a Canon α200 camera, and the back light method was employed in the experiments using a 500 -W halogen lamp. Visualization sections consist of squared boxes (filled with water) around the vertical pipe to prevent image distortion effects.

2.2.1.2 Image analysis method. The image analysis is based on the individual bubble sampling approach proposed by Aloufi [25] for a small-diameter bubble column. In this approach, each bubble is approximated and reconstructed using an ellipse (Fig. 3), represented by the following equation:

$$c_1x^2 + c_2xy + c_3y^2 + c_4x + c_5x + 1 = 0 \tag{2}$$

The method is structured in three phases:

(1) *Calibration*: The reference conversion factor between pixels and millimeters is provided.
(2) *Bubble reconstruction*: For each bubble, six points are selected on the bubble edge, and the ellipse equation parameters c_1, c_2, c_3, c_4, and c_5 are evaluated by using the least squares method.
(3) *Bubble processing*: The equivalent ellipse is processed to obtain the major axis, $2a$, and the minor axis, $2b$ (Fig. 3(*a*)). Hence, the bubble equivalent diameter, d_{eq}, and the aspect ratio, φ, are obtained

$$d_{eq} = 2\sqrt[3]{a^2b} \tag{3}$$

$$\varphi = \frac{b}{a} \tag{4}$$

The number of bubbles to be sampled to have a reliable BSD is a matter of discussion in the literature [26]. Different studies have sampled a different number of bubbles: between 50 and 100 [27], 200 [28], 250 [29], 300 [30] and between 250 and 300 [25]. In this study, 2590 bubbles have been selected using 32 photos taken to obtain time-averaged results. All of the images have been taken at approximately 2.5 m from the air distributor.

The focus of the camera (1/1200 s, ISO400, f/3.5) was adjusted on the external diameter of the inner pipes (the midplane of the column). This value is then used for the correction to the real size of the bubbles. Of course, an uncertainty exists in adjusting the focus of the camera on the column midplane; therefore, we have

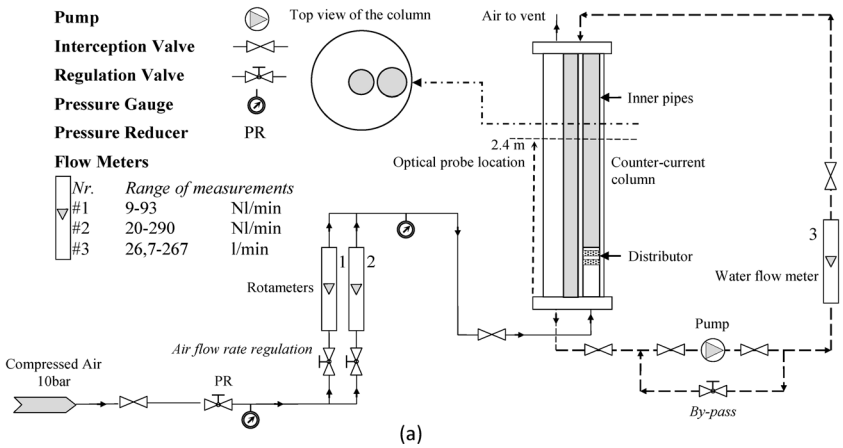

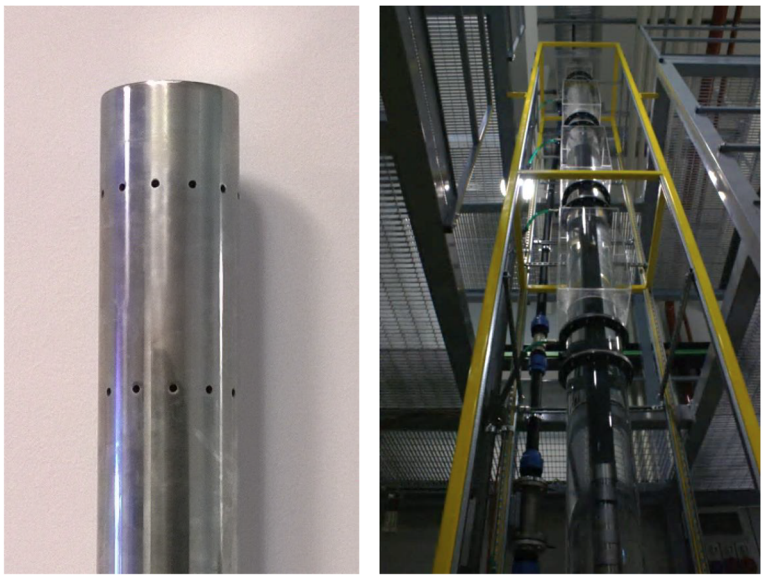

Fig. 1 Experimental facility details: (*a*) experimental facility, (*b*) air distributor, and (*c*) photo of the facility

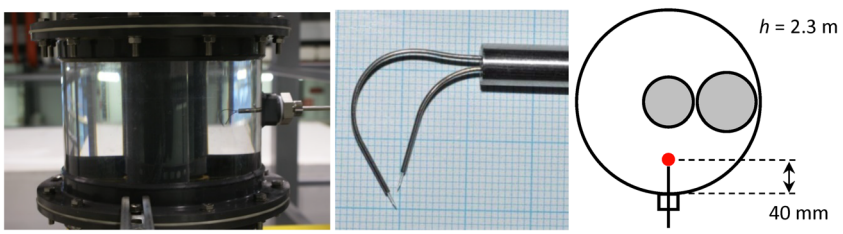

Fig. 2 The optical probe and its position within the pipe cross section

selected a region in which all of the bubbles can be considered at the same focal distance as the external diameter of the pipes. This region is defined by a line at a distance x from the center of the column (Fig. 3(*b*)). For the choice of the value of x, two factors have been taken into account:

(1) Increasing x, the area of sampling becomes smaller and the bubbles are closer to the reference plane;
(2) increasing x decreases the number of bubbles to be analyzed.

After a preliminary analysis, the value of $x = 0.3\ d_{\text{inner}}$ was chosen. This area is colored in gray in the schematic drawing of the column (Fig. 3(*b*)). It is worth noting that the BSD obtained here might not represent the true BSD in the bubble column because another BSD could be expected near the inner pipes.

2.2.2 Gas Holdup Measurements. Measurements of the bed expansion allowed the evaluation of the gas holdup ε_G. The procedure involves measuring the location (height) of the liquid free-surface when air flows in the column. The gas holdup is then obtained using the relation

$$\varepsilon_G = \frac{(H_D - H_0)}{H_D} \tag{5}$$

where H_D and H_0 are the heights of the free surface after and before aeration, respectively. The height is measured using a

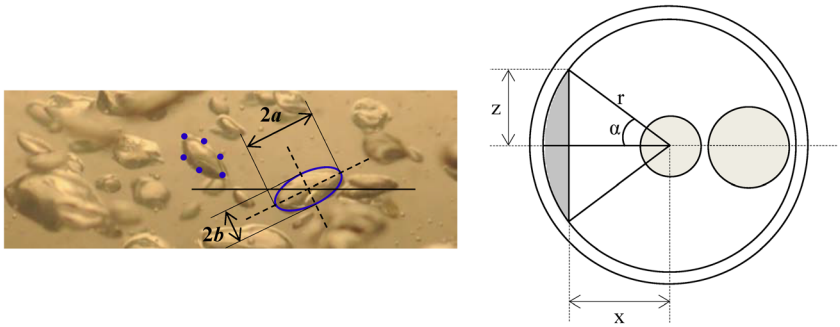

Fig. 3 Image processing: (*a*) bubble sampling and (*b*) sampling area (top view of the column)

reference position above the air distributor, where the two-phase flow is developed. The reference position is determined by measuring the location where the bubbles are spread across the entire cross section of the pipe. The error in the holdup measurements is approximately 10%. This value is in agreement with the literature [31].

2.2.3 Optical Probe Measurements

2.2.3.1 Instrumentation. A double fiber optical probe system, manufactured by RBI (Meylan, France), measures local flow properties (local void fraction, bubble vertical velocity, bubble Sauter mean diameter, interfacial area concentration, and bubble chord length distributions). Each double probe is made of two 40-μm glass fibers, whose tips are re-enforced by two sharp sapphire pins. Further information concerning this equipment can be found in Boes and Hager [32].

Optical probes distinguish the gas and liquid phases by measuring the intensity of a laser light that is reflected and/or refracted at the probe tip on the basis of the refractive indices of the probe tip, gas and liquid phases [33]. The probe signal is measured via an optoelectronic module that emits the laser to the probe tip and converts the reflected optical signal into a digital signal. From the digital signal, the bubble frequency f (bubble number per unit time) and void fraction $\varepsilon_{G,\text{Local}}$ (assuming it equals the proportion of time when the tip is surrounded by gas) can be obtained. By cross-correlating the signals from the two tips, bubble traveling time from one tip to the other can be estimated and the bubble velocity u_b can be calculated. Assuming that bubbles are spherical, the bubble-specific interfacial area, a_i, and bubble Sauter mean diameter, d_b, are calculated by the optical probe system

$$a_i = 4f/u_b \tag{6}$$

$$d_b = 3\varepsilon_{G,\text{Local}} u_b / 2f \tag{7}$$

Equation (7) is based on the assumption of spherical bubbles; however, this assumption is only approximately valid when bubbles are small. The following equation has been used to account for the nonsphericity of bubbles [34]:

$$d_{b,\text{corrected}} = \varphi^{-2/3} 3\varepsilon_{G,\text{Local}} u_b / 2f \tag{8}$$

where φ is the aspect ratio.

In the present investigation, optical probe measurements were performed both in the bubbly and in the churn turbulent flow for four water superficial velocities:

- $J_L = 0$ m/s and $J_G = 0.0087$, 0.0220, 0.0313, 0.0408, 0.1192, and 0.1987 m/s;
- $J_L = -0.04$ m/s and $J_G = 0.0087$, 0.0198, 0.0290, 0.0410, 0.1192, and 0.1981 m/s;
- $J_L = -0.08$ cm/s and $J_G = 0.0131$, 0.0220, 0.0408, 0.1189, and 0.1983 m/s; and
- $J_L = -0.11$ cm/s and $J_G = 0.0109$, 0.0198, 0.0408, 0.1186, and 0.1974 m/s.

The acquisitions are performed using a sampling period equal to $\Delta t_{\text{sampling}} = 1000$ s, which is large enough to produce reliable time-averaged values.

2.2.3.2 Optical probe errors. There are some potential sources of errors when characterizing bubbles using optical probes [35]:

- Improper dewetting at the probe tip (the *blinding effect*);
- alteration of bubble trajectory prior to or during the piercing process (the *drifting effect*); and
- bubble deformation and/or deceleration at the probe tip (the *crawling effect*).

The effect of these contributions over the local measurements is a matter of study:

- *Void fraction*: Comparing optical probe results with other measurement techniques (i.e., visual or pressure sensors), it is generally found that the underestimation of the local value and the relative differences is between −0.8% and −16% [33,36–39]. It is worth noting that Simonnet et al. [34] observed an overestimation of the optical probe value of +12%. Moreover, Barrau et al. [33] observed the worst performance with no liquid flow and/or at low gas fractions.
- *Bubble diameter*: The assumption of spherical bubbles leads to an underestimation of the equivalent diameter between +10% and 27% [36,38,40]. Applying a correction based on the aspect ratio evaluation can reduce the error, e.g., from +26.6% to +7% [36].
- *Bubble rise velocity*: The rise time errors are primarily affected by the impact angle of the bubbles with the probe tip. The relative difference reported in the literature, compared with other techniques (e.g., image processing), is between +5% and +30% [34,36–40]. Cartellier and Barrau [41] reported a higher error (+45%).

3 The Numerical Model

The numerical model used to predict the two-phase fluid dynamics in the column has been implemented in the commercial software ANSYS FLUENT release 15.0.7. The model is described briefly in Secs. 3.1 to 3.7. The modeling approach is focused on the $J_L = 0$ m/s operating condition in the bubbly flow regime, and the goal is to assess a numerical model able to simulate an annular gap configuration. In future works, the countercurrent operating conditions will be studied.

3.1 Geometrical Domain. The simulations are performed using a geometric representative of the real column geometry, i.e., a 0.24 m inner diameter pipe with two inner pipes of 0.060 m and 0.075 m outer diameters. The height of the domain is 5 m. The sparger is modeled as a uniform cylindrical surface with a height

of 0.10 m placed on the lateral inner pipe at the vertical position of 0.35 m from the bottom of the domain. For the position of the inner pipes, refer to Figs. 1–3.

3.2 Governing Equations. An Eulerian two-fluid approach is adopted in the present numerical simulations. Within such a framework, two sets of Navier–Stokes equations are ensemble-averaged, and the effects of turbulence and interphase phenomena are taken into account using closure models [42]. For an isothermal flow without mass transfer, the URANS governing equations for the kth phase are

$$\frac{\partial}{\partial t}(\alpha_k \rho_k) + \nabla \cdot (\alpha_k \rho_k \mathbf{u}_k) = 0 \tag{9}$$

$$\frac{\partial}{\partial t}(\alpha_k \rho_k \mathbf{u}_k) + \nabla \cdot (\alpha_k \rho_k \mathbf{u}_k \mathbf{u}_k) = -\alpha_k \nabla p + \nabla \cdot (\alpha_k \bar{\tau}_k) + \alpha_k \rho_k \mathbf{g} + \mathbf{M}_{I,k} \tag{10}$$

The terms on the right-hand side of Eq. (4) represent the pressure gradient, the stresses (viscous and Reynolds), the body forces, and the interfacial momentum exchanges between the phases, respectively. The last term comprises several independent physical mechanisms: drag, lift, virtual mass, turbulent dispersion, and wall lubrication forces

$$\mathbf{M}_{I,k} = \mathbf{F}_{D,k} + \mathbf{F}_{L,k} + \mathbf{F}_{\mathrm{VM},k} + \mathbf{F}_{\mathrm{TD},k} + \mathbf{F}_{\mathrm{WL},k} \tag{11}$$

In the present paper, two classes of bubbles are considered to take into account the different dynamics between small bubbles and large bubbles. As a result, the water is represented as a continuous phase, and air is modeled through two dispersed phases with a different average bubble diameter. This type of approach has been used successfully to simulate bubble columns in previous studies [14,20].

3.3 Interfacial Momentum Exchanges. Modeling and validation of forces acting on a bubble have been intensively studied over the last decade. All forces act together to produce observable phenomena, such as the distribution of the void fraction. Hence, an independent validation of each single force is not possible. Therefore, a complete set of interfacial forces should be used. A complete discussion of this approach can be found in the paper of Rzehak and Krepper [43]. The drag, lift, turbulent dispersion, and wall lubrication forces are implemented in the numerical model for both the bubble classes. The expression for these forces will be given for a dispersed phase j in a continuous phase k (water, in this study). The source term for the continuous phase is then equal to the negation of the sum of the dispersed phase source terms

$$\mathbf{F}_k = -\sum_{j=1}^{2} \mathbf{F}_j \tag{12}$$

3.3.1 Drag Force. The drag force originates from the presence of a slip velocity between the gas and liquid phases. The implementation of the drag force within the ANSYS FLUENT software gives

$$\mathbf{F}_{D,j} = -\frac{3}{4}\alpha_j(1-\alpha_j)\rho_k \frac{C_D}{d_j}|\mathbf{u}_j - \mathbf{u}_k|(\mathbf{u}_j - \mathbf{u}_k) \tag{13}$$

The drag coefficient between the continuous phase and the dispersed phases, C_D, is computed using the correlation of Tomiyama et al. [44], well suited for bubbly flows

$$C_D = \max\left[\min\left(\frac{24}{\mathrm{Re}_b}(1+0.15\mathrm{Re}_b^{0.687}), \frac{72}{\mathrm{Re}_b}\right), \frac{8}{3}\frac{\mathrm{Eo}}{\mathrm{Eo}+4}\right] \tag{14}$$

In this formulation, C_D depends on the bubble Reynolds number

$$\mathrm{Re}_b = \rho_k |\mathbf{u}_j - \mathbf{u}_k| d_j / \mu_k \tag{15}$$

and the Eötvös number

$$\mathrm{Eo} = g|\rho_k - \rho_j| d_b^2 / \sigma_{jk} \tag{16}$$

No drag force interaction is taken into account between the two dispersed phases.

3.3.2 Lift Force. The lift force is a lateral force originating in a shear flow. It is implemented as

$$\mathbf{F}_{L,j} = -C_L \alpha_j \rho_k (\mathbf{u}_j - \mathbf{u}_k) \times (\nabla \times \mathbf{u}_k) \tag{17}$$

The lift coefficient C_L depends mainly on the shape of the bubble. For small bubbles, it is positive; for deformed bubbles, it changes its sign. To account for this dependency, the model of Tomiyama et al. [44] is used to compute the lift coefficient together with the use of two bubble classes as introduced previously. One of the bubble classes represents small and nearly spherical bubbles with a positive C_L, while the other one models large and deformed bubbles with a negative C_L. For the air–water system at ambient conditions, the bubble diameter at which the change in sign occurs is 5.8 mm. The lift coefficient according to Tomiyama et al. is given as

$$C_L = \begin{cases} \min[0.288\tanh(0.121\mathrm{Re}_b),\ f(\mathrm{Eo}_\perp)] & \mathrm{Eo}_\perp \le 4 \\ f(\mathrm{Eo}_\perp) & 4 < \mathrm{Eo}_\perp \le 10 \\ -0.27 & 10 < \mathrm{Eo}_\perp \end{cases} \tag{18}$$

with

$$f(\mathrm{Eo}_\perp) = 0.00105\mathrm{Eo}_\perp^3 - 0.0159\mathrm{Eo}_\perp^2 - 0.0204\mathrm{Eo}_\perp + 0.474 \tag{19}$$

where $\mathrm{Eo}_\perp$ is the Eötvös number considering the maximum horizontal dimension of the bubble $d_\perp$ given by the empirical correlation for the aspect ratio by Wellek et al. [45]

$$d_\perp = d_b(1 + 0.163\mathrm{Eo}^{0.757})^{1/3} \tag{20}$$

3.3.3 Turbulent Dispersion Force. The diffusion effect of the turbulent fluctuations of the liquid phase on the bubbles is modeled through the turbulent dispersion force. It is derived by Favre averaging the interphase drag term. The model of Burns et al. [46] is implemented and reads as

$$\mathbf{F}_{\mathrm{TD},j} = -\frac{3}{4}C_{\mathrm{TD}}\alpha_j(1-\alpha_j)\frac{C_D}{d_j}|\mathbf{u}_j - \mathbf{u}_k|\frac{\mu_k^{\mathrm{turb}}}{\sigma_{\mathrm{TD}}}\left(\frac{\nabla\alpha_j}{\alpha_j} - \frac{\nabla\alpha_k}{\alpha_k}\right) \tag{21}$$

where $C_{\mathrm{TD}} = 1$ and $\sigma_{jk} = 0.9$.

3.3.4 Wall Lubrication Force. A bubble moving near a wall is subject to a lift force that pushes it away from the wall. This force is often mentioned as the wall lubrication force and is implemented as

$$\mathbf{F}_{\mathrm{WL},j} = -C_{\mathrm{WL}}\rho_k\alpha_j\left|(\mathbf{u}_k - \mathbf{u}_j)_{||}\right|^2 \mathbf{n}_w \tag{22}$$

where $(\mathbf{u}_k - \mathbf{u}_j)_{||}$ is the relative velocity component parallel to the wall and $\mathbf{n}_w$ is the unit normal to the wall pointing toward the fluid. C_{WL} is the wall lubrication coefficient, which depends

mainly on the distance to the wall and is given here by the model of Antal et al. [47]

$$C_{\mathrm{WL}} = \max\left(0, \frac{C_{W1}}{d_b} + \frac{C_{W2}}{y_W}\right) \tag{23}$$

where $C_{W1} = -0.01$ and $C_{W2} = 0.05$ are dimensionless constants and y_W is the distance to the nearest wall.

3.4 Turbulence Modeling. In this study, we have used an eddy diffusivity approach for the turbulence modeling. The two equation k-ω shear-stress-transport model is used to include the effect of turbulence, as suggested in Refs. [14,20,43]. The constants of the model follow their single phase values. Turbulence effects in the liquid phase induced by the bubbles have been neglected.

3.5 Numerical Settings. Three-dimensional transient simulations have been carried out. The numerical simulations are performed on a mesh of 180,000 hexahedral cells. Each cell is approximately $12 \times 12 \times 12$ mm^3. A grid resolution study was conducted to ensure that convergence with respect to the spatial resolution has been achieved. The various numerical schemes are chosen to reduce the discretization error as much as possible within the ANSYS FLUENT CFD software. A second-order Euler implicit temporal discretization scheme is adopted. Gradients are estimated using a least squares cell-based method. The quadratic upstream interpolation for convective kinematics scheme is used to discretize the convection term of each scalar solved. A phase coupled semi-implicit method for pressure-linked equations algorithm guarantees the coupling between pressure, velocity, and volume fraction. The time discretization is characterized by using the CFL number and, in this study, a CFL ≈ 0.10 is considered: the resulting time step size is $\Delta t = 0.0005$ s. The iterations within each time step are stopped when the residuals fall below 10^{-5}.

3.6 Simulation Procedure. The simulation procedure is similar to the typical one employed for studying transient bubble column flow [14,15,17,18,20]. The sequence followed in the simulations includes an initial run to reach a statistical steady temporal convergence of the solution. The first run has the duration of 30 s in physical time, and a second run of 120 s is performed with data sampling to collect temporal averages and deviations of the fluid dynamic parameters. The choice of the duration of the first run is dictated by the temporal evolution of the total gas holdup, i.e., within the entire computational domain. When this quantity stabilizes, it means that the flow is developed and that data sampling operations can be performed. The analysis on the simulation procedure was previously discussed by Besagni et al. [48].

3.7 Materials and Boundary and Initial Conditions. Despite the air phase having a slightly varying density from the bottom to the top of the column, both fluids are considered incompressible. A hydrostatic pressure variation of 0.3 bar exists from the air distributor until the free surface; thus, the air density is taken at the averaged conditions $p = 1.15$ bar and $T = 20\,^{\circ}$C. The resulting density of air and water is 1.38 kg/m^3 and 1000 kg/m^3, respectively. The dynamic viscosity of air and water is assumed to be 1.8×10^{-5} Pa·s and 1.0×10^{-3} Pa·s, respectively. The surface tension coefficient, required for the calculation of the drag coefficient, is set to 0.072 N/m. Two cases with different superficial air velocities are investigated: (1) $J_G = 0.0087$ m/s and $J_L = 0$ m/s (case A) and (2) $J_G = 0.0228$ m/s and $J_L = 0$ m/s (case B). These operating conditions lie in the bubbly flow regimes, and in particular, case B lies just before the flow regime transition (Sec. 4.3). Velocity inlet boundary conditions are assigned at the air distributor, and the pressure is assigned at the outlet. At the walls, a no-slip boundary condition is applied for the continuous phase and a free-slip condition for the disperse phase.

3.8 Bubble Size. Simulations taking polydispersity into account have been performed by modeling the discrete phase by means of multiple classes. The bubble mean diameter of each bubble class is set according to the experimental measurements of the bubble diameter distribution for case A (refer to the image analysis in Sec. 4.1 for the detailed results). This BSD is used also for case B because of the similar bubble chord distribution obtained by the optical probe (refer to Sec. 4.5). In the homogenous regime of a bubble column, the coalescence and breakup can be neglected [49]. Moreover, two or three velocity classes can describe the main effects of the bubbly flow, as suggested in Ref. [50]. In the present investigation, to keep the numerical effort small, two bubble classes are considered. The subdivision into two classes is performed by distinguishing the bubbles having a negative lift coefficient from those having a positive lift coefficient. According to the literature, the change in lift force direction occurs at a bubble diameter of 5.8 mm for the air–water system at ambient conditions. Splitting the distribution yields two distributions with diameters below and above 5.8 mm. The Sauter mean bubble diameter and the relative frequency of the two bubble classes can be calculated as

$$d_b = \frac{\sum_i^N n_i d_{Bi}^3}{\sum_i^N n_i d_{Bi}^2} \tag{24}$$

where d_{Bi} and n_i are the diameter and the number of bubbles of size class i, respectively, and N is the number of classes used for the distribution. As a result, at the inlet, two dispersed phases are implemented: a small-diameter bubble class ($d_b = 4.18$ mm) and a large-diameter bubble class ($d_b = 7.38$ mm). It is worth noting that these two classes have a mean diameter value different from the peaks observed in the experimental BSD obtained from digital images (refer to Sec. 4.1). The resulting data are summarized in Table 1 and are used in the simulations of both cases A and B.

4 The Experimental Results

Herein, the experimental results are detailed. First, flow configurations, qualitative information on fluid dynamics, and information on bubble diameter distribution have been obtained via digital images. Second, the holdup measurements are presented and used to obtain information on the global hydrodynamics of the system. Third, optical probe data are presented and used to investigate the local flow behavior.

4.1 Flow Regimes Description and Discussion. Ranging from low to high air superficial velocity, the homogeneous-bubbly flow, a transition zone, and the heterogeneous-churn turbulent flow were observed. In the bubbly flow regime (Fig. 4(*a*)), bubbles are uniformly distributed in the cross section of the pipe, traveling vertically with minor transverse and axial oscillations. Around the inner pipes, flow recirculation and the periodic appearance of cap bubbles occur. The cap bubbles seem to originate from the bubble coalescence around the inner pipes. Due to the presence of these cap bubbles, this regime can be defined as a pseudo-homogeneous regime. Increasing the water flow rate, at a fixed superficial gas velocity, the bubble rise velocity decreases and the number of bubbles increases (Fig. 5).

Table 1 Bubble classes used in the simulations

	d_b (mm)	α	$\mathrm{Eo}_\perp$	C_L
Small bubble class	4.18	0.88	2.82	0.288
Large bubble class	7.38	0.12	10.6	−0.270

The bubble diameter distribution in the bubbly flow regime ($J_G = 0.0087$ m/s and $J_L = 0$ m/s) obtained from the image analysis is a bimodal distribution (Fig. 6(*a*)) having two peaks: the first one at the low diameter $d_{eq} = 0.5$–1 mm and the second one at $d_{eq} = 3$–3.5 mm. Such a bimodal distribution has been noticed in other studies from the literature [28,51–53]. The Sauter mean bubble diameter is (Eq. (24)) $d_b = 5.26$ mm. As expected, a relation between the size of the bubbles and the aspect ratio seems to exist: the small bubbles have high aspect ratio (closer to a spherical shape), while the larger bubbles seem to be characterized by lower aspect ratio (Fig. 6(*b*)). Indeed, bubbles with an equivalent diameter less than 1 mm tend to be spherical, having an aspect ratio greater than 0.7. Bubbles with higher equivalent diameter are characterized by a lower aspect ratio (between 0.4 and 0.7), showing the trend of larger bubbles to be more flattened.

By increasing air flow rate from the bubbly flow regime, the coalescence rate increases leading to a transition regime (Figs. 4(*b*) and 4(*c*)) toward the heterogeneous (churn turbulent) regime (Figs. 4(*d*) and 4(*e*)), and finally, a fully developed churn turbulent regime is reached (Fig. 4(*f*)) and large periodic eddies accompanied with flow recirculation are observed all along the vertical development of the pipe. This flow regime is similar to the one encountered in the annular gap configuration documented in previous studies [54]: the gas is moving continuously upward, and large bubbles that occupy the major part of the cross section of the pipe lift the liquid to a certain height. The liquid then falls, accumulates, and bridges the two tubes of the annulus and is lifted up by the gas again. By increasing the water flow rate, the bubble number increases and the bubble rising velocity decreases.

The absence of a stable slug flow can be explained by large-diameter pipe theory: the dimensionless diameter is $D_H^* = 88.13$ (above the critical value), without considering the internal pipes, and $D_H^* = 47.37$ (below the critical value) in the annular gap configuration. Hence, this facility considers an intermediate pipe that originates from a large-diameter pipe; therefore, stable Taylor bubbles have not been detected because of the above-discussed instabilities. Moreover, in a large-diameter pipe, high turbulence is expected, and in the present case, bubble coalescence and breakup constantly occur even at low gas flow rate. The high flow mixing is the reason why the flow field rapidly becomes developed: a distance of approximately 5–7 d_{inner} is required for the flow to develop downstream from the air distributor. Accordingly, the double optical probe measurements are taken at approximately 8 d_{inner} from the air distributor.

4.2 Gas Holdup. The gas holdup data have been measured for superficial air velocities up to 0.23 m/s and superficial water velocities up to −0.11 m/s (Fig. 7). At low air superficial velocity, in the bubbly flow regime, the relation between the gas holdup and the air superficial velocity is linear, followed by a change in slope due to the flow regime transition toward the bubbly–churn transition zone. By increasing the liquid flow rate, a faster increase in the holdup is observed at low superficial gas velocities, and the transition point also moves toward lower superficial gas velocities. This is explained by the effect of the liquid flow, which slows down the rise of the bubbles, leading to higher holdup. The more compact arrangement of the bubbles leads to an earlier flow regime transition. Above the transition velocity, large deformed bubbles start to appear, and the bubble coalescence increases the average rise velocity and reduces the gas residence time in the column, hence decreasing the gas holdup versus gas velocity slope.

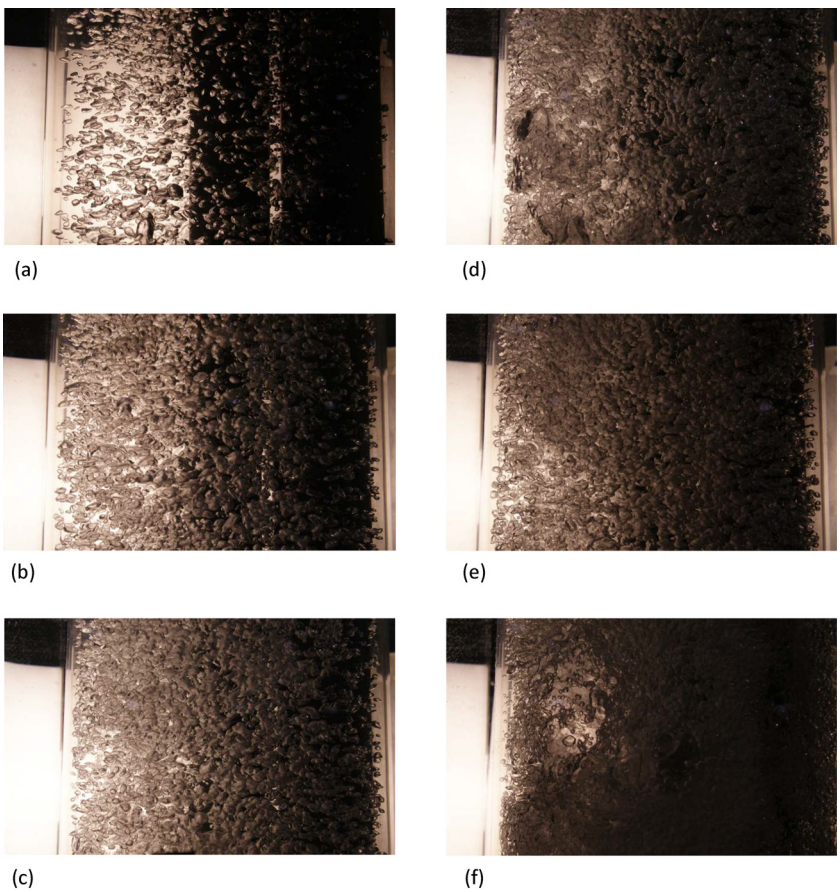

Fig. 4 Photographs of the air–water flow at $h = 2.8$ m—influence of the superficial gas velocity: $J_L = 0$ m/s and (*a*) $J_G = 0.0087$ m/s, (*b*) $J_G = 0.0220$ m/s, (*c*) $J_G = 0.0313$ m/s, (*d*) $J_G = 0.0408$ m/s, (*e*) $J_G = 0.1192$ m/s, and (*f*) $J_G = 0.1986$ m/s

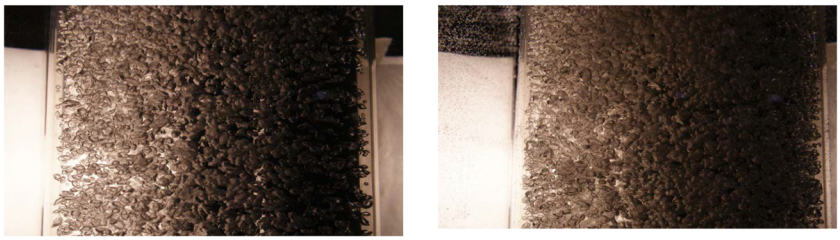

Fig. 5 Photographs of the air–water flow at $h = 2.8$ m—influence of the superficial liquid velocity: $J_G = 0.220$ m/s and (*a*) $J_L = 0$ m/s; (*b*) $J_L = -0.08$ m/s

Above $\varepsilon_G \approx 16$–17%, the water superficial velocity has no influence on the gas holdup. The discrepancy of the holdup in the heterogeneous regime between the no liquid flow and the countercurrent configurations is hardly justified. A possible hypothesis may be the asymmetric distributor, which generates a larger flow development zone in the no liquid flow configuration with respect to the countercurrent cases, due to the lower liquid back-mixing.

Otake et al. [55] observed an increase in the holdup and earlier regime transitions as the countercurrent liquid flow rate is increased in a small pipe with a diameter of 0.05 m. Their analysis covered gas superficial velocities up to 0.0824 m/s and liquid superficial velocities up to −0.15 m/s. Similar conclusions were drawn by Yamaguchi and Yamazaki [3] for small pipes with diameters of 0.04 m and 0.08 m, with gas superficial velocities up to 1 m/s. On the contrary, Akita and Yoshida [56] observed that the liquid flow rate had no influence in a large pipe with a diameter of 0.152 m at gas superficial velocities up to 0.032 m/s and liquid superficial velocities up to 0.04 m/s. The latter is in disagreement with what we observed in the bubbly flow regime, while the former suggests an influence of liquid flow rate at gas superficial velocities higher than 0.06 m/s.

4.3 Flow Regime Transition. The flow regime transition from bubbly flow to the transition zone can be predicted by analyzing the swarm rise velocity $U_{\text{swarm}} = J_G/\varepsilon_G$ with respect to the superficial gas velocity (Fig. 8(*a*)), as proposed by Krishna et al. [57]. The swarm velocity is constant in the homogeneous regime, but it starts to increase as the system enters the heterogeneous regime at a certain transition superficial velocity. The appearance of the first large bubble is responsible for a very sudden increase in swarm velocity and is an indication of flow regime transition. The transition gas velocity U_{trans} can be determined by the intersection between the two trends of holdup in the two flow regimes (Fig. 8(*b*)). The trend in the churn turbulent flow is determined by a least squares fitting of the following function:

$$U_{\text{swarm}} = A(J_G)^B + C \tag{25}$$

where A, B, and C are parameters.

The transition velocity decreases while the liquid velocity increases, because bubbles are closer in a countercurrent operating condition. Indeed, $U_{\text{trans}} = 0.0259$ m/s for $J_L = 0$ m/s decreases when increasing the counter current liquid velocity ($U_{\text{trans}} = 0.0213$, 0.018, and 0.0168 m/s for $J_L = -0.04$, −0.08, and −0.11 m/s, respectively).

Typical values of U_{trans} found in the literature for the air–water systems in bubble columns with diameters higher than 0.15 m range between 0.01 and 0.08 m/s at ambient operating conditions [24,57–66]. The value depends mainly on the distributor type. Single and multiple nozzles or perforated plate distributors with hole diameters greater than 1 mm ("coarse" distributors) usually lead to an early regime transition, while "fine" distributors such as porous plates can maintain a stable bubbly flow at higher gas flow rates. The distributor considered in this study is of the coarse type, and values of U_{trans} are in agreement with data and observations presented in the literature. In particular, the values in the present study are in very good agreement with the studies of Dargar and Macchi [65], Rollbusch et al. [66], and Besagni and Inzoli [64].

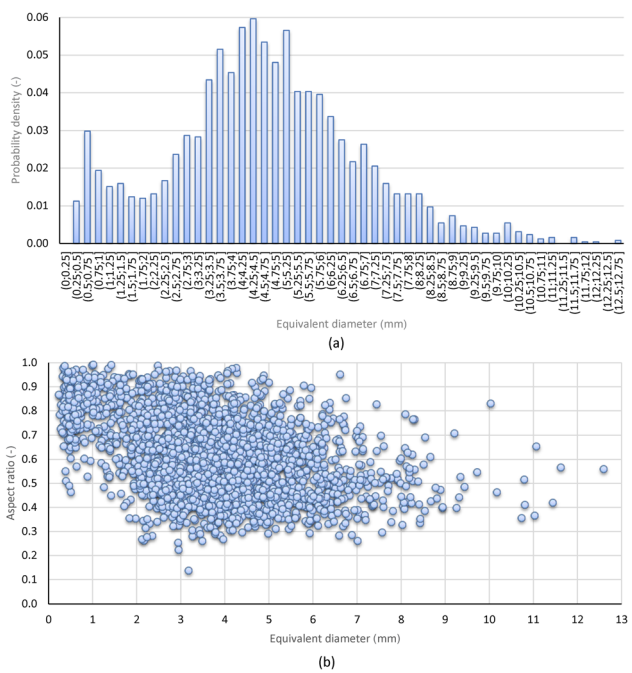

Fig. 6 Image analysis results ($J_G = 0.0087$ m/s and $J_L = 0$ m/s): (*a*) BSD and (*b*) relation between aspect ratio and equivalent diameter

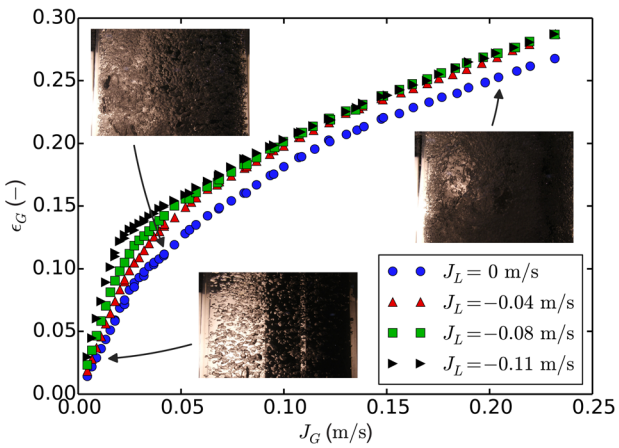

Fig. 7 Gas holdup

Some correlations for the determination of U_{trans} are available in the literature. One of the first correlations proposed is from Wilkinson et al. [59]

$$U_{trans} = 0.5U_{b,small}\exp\left(-193\rho_G^{-0.61}\mu_L^{0.5}\sigma^{0.11}\right) \tag{26}$$

with

$$U_{b,small} = 2.25\frac{\sigma}{\mu_L}\left(\frac{\sigma^3\rho_L}{g\mu_L^4}\right)^{-0.273}\left(\frac{\rho_L}{\rho_G}\right)^{0.03} \tag{27}$$

Another correlation is from Reilly et al. [24] and reads as

$$U_{trans} = \frac{\rho_L}{\rho_G}\left(1-\varepsilon_{G,trans}\right)\left(\frac{B^*}{A^*}\right)^{1.5} \tag{28}$$

with the holdup at the transition

$$\varepsilon_{G,trans} = 0.59B^{*1.5}\left(\frac{\sigma^{0.12}\rho_G^{0.96}}{\rho_L}\right)^{0.5} \tag{29}$$

and

$$A^* = 2.81\rho_L\rho_G^{0.96}\sigma^{-0.12} \tag{30}$$

For water in the liquid phase, $B^* = 3.75$. Comparisons of U_{trans} and $\varepsilon_{G,trans}$ from the experimental investigation and these correlations are given in Table 2. Equation (25) largely underestimates the transition gas velocity; this observation was also made by Letzel et al. [60], who also compared their results with the correlation of Reilly et al. [24], which provides a better agreement. Alternately, Eq. (27) gives values for U_{trans} and $\varepsilon_{G,trans}$, which are in agreement with the experimental data. Despite the experimental data lying within the ranges observed in the literature, the flow regime transition occurs quite early. This could be due to the distributor design used in the experiment, as well as due to the presence of internal pipes.

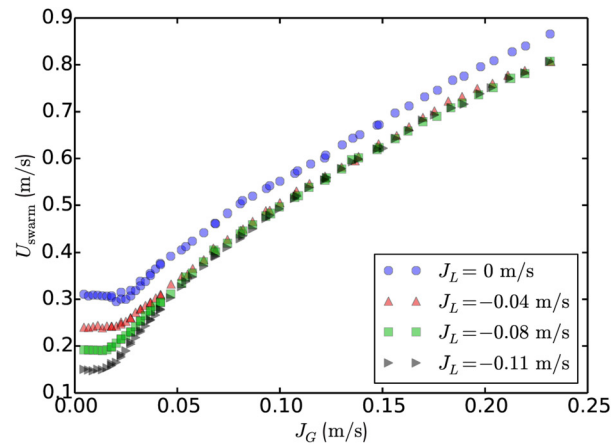

(a)

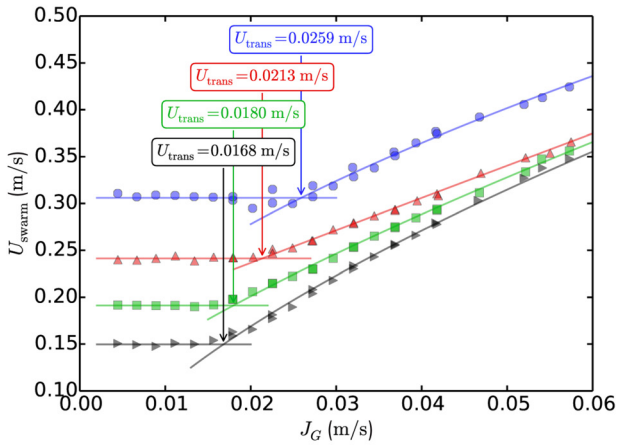

(b)

Fig. 8 (*a*) Swarm velocity and (*b*) transitions velocity

4.4 Comparison With Correlations and Data From the Literature

4.4.1 Data Comparison. In the literature, several experimental data are available for bubble columns with various diameters. However, few studies are available on countercurrent flow in large-diameter pipes. Moreover, experiments involving internal pipes in large-diameter columns are almost absent. The inner pipes may influence the trend of the holdup; thus, further investigations without the presence of the inner pipes are required. To compare the holdup data, a set of experimental studies, with a pipe diameter and sparger design similar to those considered in this study, have been selected. The list of references is reported in Table 3, and the comparison with the data is displayed in Fig. 9. The data by Al-Oufi et al. [10] refer to the annular gap configuration with an inner-tube diameter of 0.051 m. A relative high variability between the reference data is observed. However, the holdup results lie within the range of such variability, indicating that the two-phase flow dynamics in this experimental configuration are similar to those in bubble columns without inner pipes.

4.4.2 Correlations Comparison. Four correlations have been analyzed (Fig. 9): those of Reilly et al. [69], Joshi and Sharma [70], Hughmark [71], and Kawase and Murray [72]. For both low and high air superficial velocities, the correlation of Hughmark gives the better predictions. For low air superficial velocities, the correlation of Joshi and Sharma and the correlation of Kawase and Murray well predict the experimental data. The correlation of Reilly et al. gives a similar trend to that of the experimental data; however, a constant shift of volume fraction is observed.

4.4.3 Proposed Correlation for the Gas Holdup. The correlations from the literature cannot predict the holdup curve in all of the operating conditions, therefore a new correlation is proposed. The relationship between the gas holdup and the physical properties of the system may be written as a function of the following parameters:

$$\varepsilon_G = f\left(g, J_G, d_{eq}, \mu_L, \rho_L - \rho_G, g\right) \tag{31}$$

This equation can be transformed by means of the dimensional analysis

$$\varepsilon_G = f\left(\frac{J_G\mu_L}{\sigma}, \frac{g\mu_L^4}{(\rho_L-\rho_G)\sigma^3}\right) = f(\mathrm{Ca}, \mathrm{Mo}) \tag{32}$$

A different formulation can be used for the function f, and in this paper, the same expression proposed by Akita and Yoshida [56] is used

Table 2 Flow regime transition: comparison with the literature

	Experiment	Wilkinson et al. [59]	Reilly et al. [24]
U_{trans} (m/s)	0.0259	0.00198	0.0289
$\varepsilon_{gas,trans}$	0.0846[a]	0.0077[b]	0.1295

[a]The value is given by U_{trans}/U_{swarm}.
[b]The value is given by $U_{trans}/U_{b,small}$ (Eq. (27)).

Table 3 Experimental studies

	Reference	Configuration	D_c (m)	Sparger design
R1	Reith et al. [67]	Open tube	0.14	Perforated plate—$d_{holes} = 2$ mm
R2	Reith et al. [67]	Open tube	0.29	Perforated plate—$d_{holes} = 2$ mm
R3	Schumpe and Grund [58]	Open tube	0.30	Ring—$d_{holes} = 1$ mm
R4	Wilkinson et al. [59]	Open tube	0.15	Ring—$d_{holes} = 2$ mm
R5	Wilkinson et al. [59]	Open tube	0.23	Ring—$d_{holes} = 7$ mm
R6	Throat et al. [68]	Open tube	0.385	Sieve plate—$d_{holes} = 1$ mm
R7	Throat et al. [68]	Open tube	0.385	Sieve plate—$d_{holes} = 2$ mm
R8	Al-Oufi et al. [10]	Annular gap	0.102	Porous plate—$d_{holes} = 0.1$ mm

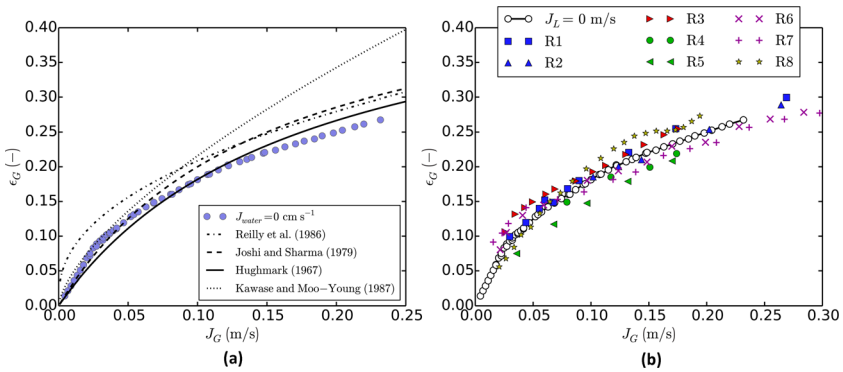

Fig. 9 Holdup measurements ($J_L = 0$ m/s): (*a*) comparison with literature correlations and (*b*) comparison with data from the literature (Table 3)

$$\frac{\varepsilon_G}{(1-\varepsilon_G)^4} = k\mathrm{Mo}^{k_1}\mathrm{Ca}^{k_2} \tag{33}$$

Being the liquid properties constant, the Mo^b term becomes constant

$$\ln\left(\frac{\varepsilon_G}{(1-\varepsilon_G)^4}\right) = k_2\ln(\mathrm{Ca}) + \ln(k^*) \tag{34}$$

which can be rewritten as

$$\ln\left(\frac{\varepsilon_G}{(1-\varepsilon_G)^4}\right) = c\ln(\mathrm{Ca}) + \ln(a^*) \tag{35}$$

It is now in the following form:

$$y = mx + q \tag{36}$$

where $k_2 = m$, $\ln(\mathrm{Ca}) = x$, and $\ln(k^*) = q$. Therefore, a linear regression can be used, resulting in ($R^2 = 0.9958$)

$$y = 0.9966x + 5.797 \tag{37}$$

Hence, $k_2 = 0.9966$ and $k^* = 329.31$.
Finally, the proposed correlation takes the following form:

$$\frac{\varepsilon_G}{(1-\varepsilon_G)^4} = 329.31\mathrm{Ca}^{0.997} \tag{38}$$

The results can be found in Fig. 10, and the proposed correlation matches the data fairly well if compared to the previous correlation in the literature.

4.5 Optical Probe Measurements. The local void fraction (Fig. 11(*a*)) increases with superficial air velocity, as expected, and with superficial water velocity. This is because bubbles move in a nonstagnant surrounding liquid, which is forced to move downward.

The bubble vertical velocity (Fig. 11(*b*)) increases with superficial air velocity, as one would expect. The increase of the bubble vertical velocity after the transition of the superficial gas velocity is due to the increased coalescence rate. The increase in the superficial water velocity also leads to an increase in the bubble vertical velocity. Furthermore, liquid may be more concentrated near walls, and an increase of liquid velocity may result in the increase of the thickness of the liquid film near the walls, resulting in the increase of the gas velocity in the core of the section.

The bubble Sauter mean diameter (Fig. 11(*c*)) increases with air flow rate. It is frequently admitted that, in a given gas injection configuration, the bubble diameter is an increasing function of the superficial gas velocity. The reasons for this increase can be linked to the coalescence phenomena [34]. We have noticed that an increasing diameter also increases the water flow rate. As discussed before, the Sauter mean diameter obtained from the optical probe refers to a spherical shape. While considering the operating conditions (analyzed using the image processing), the Sauter

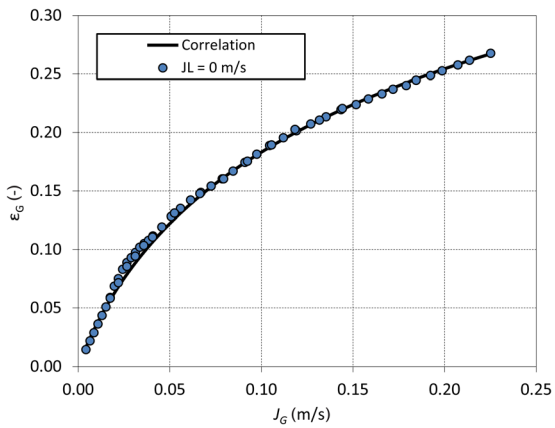

Fig. 10 Proposed correlation for the gas holdup

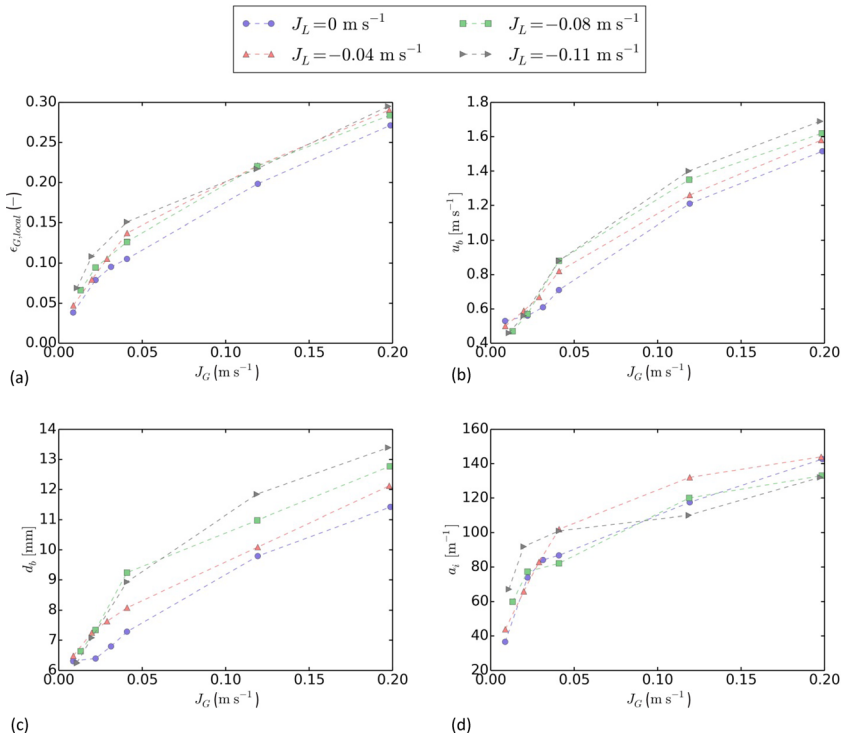

Fig. 11 Optical probe measurements: (*a*) local void fraction, (*b*) bubble velocity, (*c*) bubble Sauter mean diameter, and (*d*) interfacial area

mean diameter from the optical probe and from the image analysis is found to be 6.3 and 5.26 mm, respectively. Applying the correction previously described in Eq. (8) with a mean aspect ratio of 0.7 (mean value from the experimental data of the image analysis), the corrected Sauter mean diameter from the optical probe is 4.975 mm. The resulting error decreases and changes from −19.81% to 5.52%.

The interfacial area concentration (Fig. 11(*d*)) increases with the increase of water superficial velocity at low air superficial velocity, and an opposite trend is observed at higher air superficial velocity. This indicates that, as the bubble diameter increases, the interfacial area concentration decreases after some point.

The bubble chord distribution data are presented in Fig. 12 for the four superficial water velocities and the different superficial

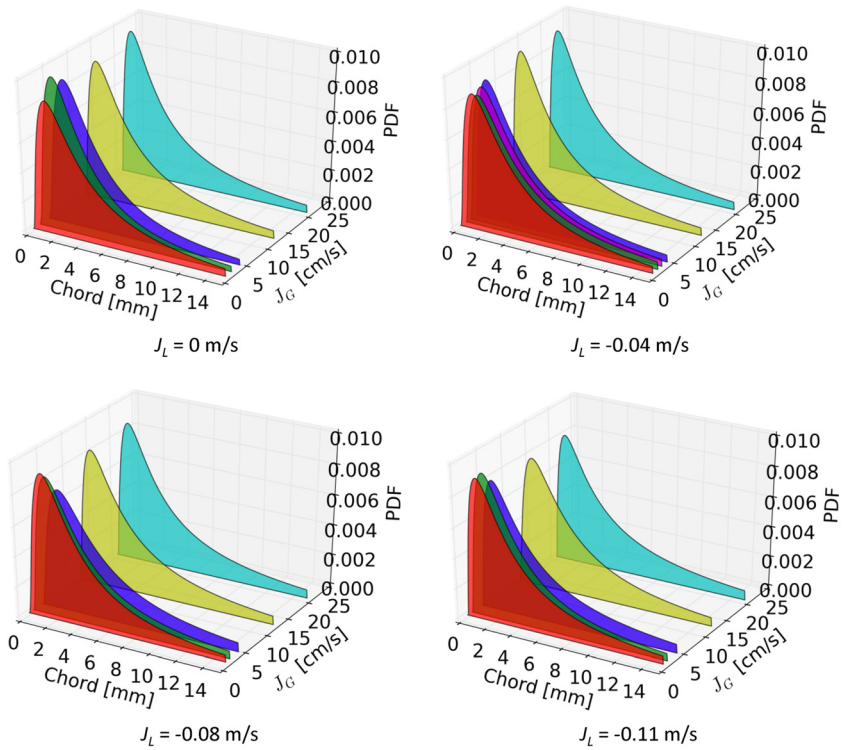

Fig. 12 Bubble chord distributions

Table 4 Numerical results: gas holdup and local void fraction comparison

Data	Model	Case A	Case B
Holdup	Experiment	2.9%	7.5%
	CFD	3.1% (+6.9%)	8.0% (+6.7%)
Local void fraction	Experiment	3.31%	8.71%
	CFD	3.85% (+16.3%)	7.89% (−9.41%)

gas velocities at which local measurements were performed. In future studies, the bubble chord distributions could be converted to BSD using correction algorithms from the literature, such as the one proposed by Hoang et al. [73].

5 The Numerical Results

Numerical results from CFD simulations are presented, discussed, and compared to experimental data. Results in terms of gas holdup, local void fraction, and cross-sectional void fraction distribution are analyzed.

5.1 Experimental Data Comparison. Gas holdups from the numerical simulations are measured in a similar way with respect to the experiments, i.e., measuring the free-surface height and comparing it with the initial water volume. The results obtained for the two cases (A and B) identified previously are summarized in Table 4. A very good agreement between the numerical results and the experiments is found, and errors in the global holdup are below 7% in the range considered. The two cases analyzed cover the bubbly flow regime (case B is just before the flow regime transition), and this suggests that the present model can predict the bubbly flow regime in the annular gap bubble column. The optical probe data have been compared with local numerical results, showing a relative error between −9% and +16%. The data used for comparison are the mean values of the void fractions. Of course, the experimental data are affected by an uncertainty, which has been discussed in Sec. 2. Such agreement is achievable only when two bubble classes are implemented. We noticed that, with only the small bubble class, the bubble plume diffuses completely within the pipe cross section and the gas holdup is largely overestimated. Alternately, with only the large bubble class, the bubble plume does not diffuse transversally and remains attached to the internal pipes, leading to qualitatively and quantitatively wrong results [48]. Instead, when two bubble classes are considered, the bubble plume starts to oscillate and to expand within the entire cross section slightly after the air distributor. This behavior, together with the development length, matches very well the experimental observations.

5.2 Cross-Sectional Volume Fraction Distribution. The qualitative visualization of the cross-sectional volume fraction distribution allows a better understanding of the quality of the predictions. In Fig. 13, the time-averaged air volume fraction distribution (mean air volume fraction; the sum of the small and large bubbles phases) is shown for various vertical positions ranging from 0.8 to 3.3 m. Few changes of the cross-sectional air volume fraction distribution are noticed from the vertical position $h = 2.0$ m until $h = 3.0$ m, suggesting that the two-phase flow develops quite rapidly as in the experiments. A similar flow development is also observed for case B, as shown in Fig. 14. In Fig. 15, the time-averaged volume fraction distribution of the water and the small bubbles and large bubbles phases is displayed for cases A (Fig. 15(*a*)) and B (Fig. 15(*b*)) within the horizontal plane at $h = 2.3$ m. A concentration of the large bubbles phase is noticed near the inner pipes for both cases. Alternately, the small

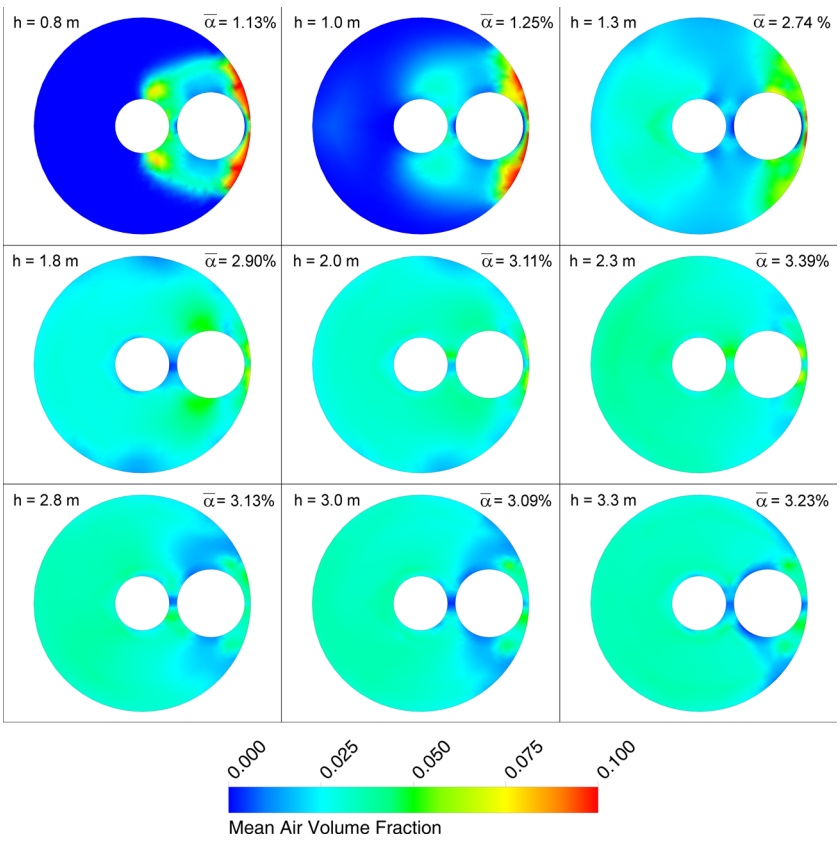

Fig. 13 Cross-sectional contour of time-averaged air volume fraction at various vertical positions for case A (values of the area-averaged air volume fraction are also displayed)

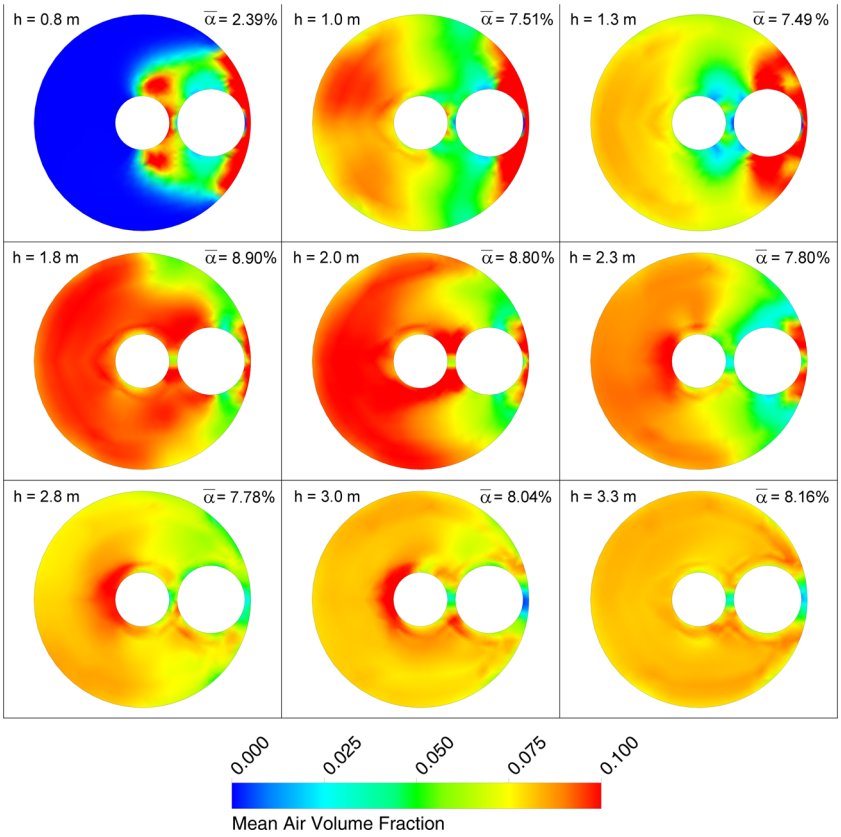

Fig. 14 Cross-sectional contour of time-averaged air volume fraction at various vertical positions for case B (values of the area-averaged air volume fraction are also displayed)

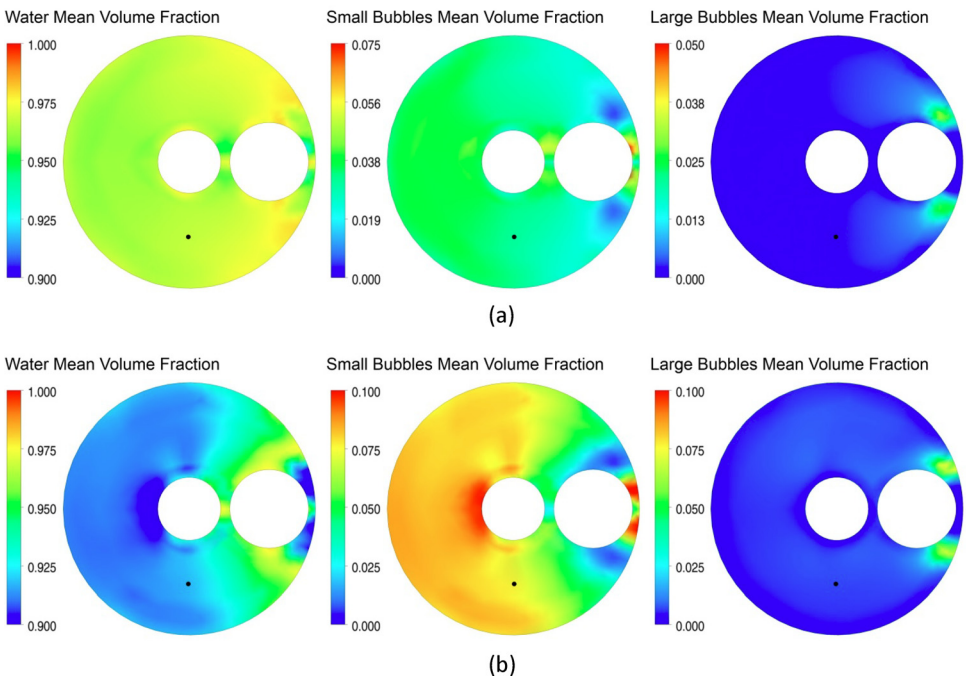

Fig. 15 Cross-sectional contour of time-averaged volume fraction at the horizontal plane $h = 2.3$ m (the black dot indicates the probe location for local measurements): (*a*) case A and (*b*) case B

bubbles phase tends to spread within the entire cross section, which is also consistent with the experiments where a homogeneous-bubbly flow is witnessed far from the inner pipes.

6 Conclusions

This paper investigates the countercurrent gas–liquid flow in an annular gap bubble column with an inner diameter of 0.24 m via experimental and numerical investigations.

In the first part, the experimental results are detailed. A homogeneous-bubbly flow regime and a heterogeneous-churn turbulent flow regime have been reported, with a transition zone between the two regimes. The stable slug flow, the annular flow, and the flooding condition were not observed, and the absence of slug flow is motivated by the theoretical consideration of large-diameter pipes. In the homogeneous regime, bubble recirculation occurs around the inner pipes, along with the periodic appearance of cap bubbles. In the bubbly flow regime, gas holdup increases linearly as a function of the gas flow rate, and it increases with the water flow rate; however, in the heterogeneous regime, the water superficial velocity has no influence on the holdup. The flow regime transition toward the heterogeneous regime has been quantitatively analyzed using holdup measurements. A comparison between holdup measurements and literature correlations has revealed that the present experimental data are in agreement with the previous studies in the literature. Local flow behavior has been analyzed considering the local void fraction, the bubble velocity, the bubble diameter, and the bubble chord distributions.

In the second part, a CFD modeling of the column operating in the bubbly flow regime is proposed using the commercial software ANSYS FLUENT. Three-dimensional transient simulations have been performed considering a set of nondrag forces and polydispersity within an Eulerian two-fluid approach. It is shown that the errors in the global holdup and in the local properties are below 7% and 16%, respectively, in the range considered. Further studies may concern the influence of the inner pipes on the flow behavior and analysis of the images to provide further data concerning the bubble shape and its influence on the global fluid dynamics parameters.

Nomenclature

a_i = interfacial area concentration (m^2/m^3)
BSD = bubble size distribution
c = coefficient in the ellipse equation
C_D = drag coefficient
C_L = lift coefficient
Ca = $J_G\mu_L/\sigma$ capillary number
CFD = computational fluid dynamics
CFL = Courant–Friedrichs–Lewy number
d_b = bubble Sauter mean diameter (mm)
d_{eq} = equivalent bubble diameter (mm)
d_{holes} = diameter of holes (m)
d_{inner} = inner diameter of pipes (m)
D_H = hydraulic diameter (m)
D_H^* = dimensionless hydraulic diameter
$D_{H,cr}^*$ = critical dimensionless hydraulic diameter
Eo = $g|\rho_k - \rho_j|d_b^2/\sigma_{jk}$ Eötvös number
f = bubble frequency (1/s)
g = gravity acceleration (m/s^2)
h = vertical position (m)
H = pipe height (m)
H_D = height of water free-surface after aeration (m)
H_0 = initial height of water free-surface (m)
J = superficial velocity (m/s)
k = coefficient in the holdup correlation
m = coefficient in the holdup correlation
$\mathbf{M}_I$ = momentum exchanges ($kg/(m^2\ s^2)$)
Mo = $g\mu_L^4/(\rho_L - \rho_G)\sigma^3$ Morton number
n = refractive index
p = pressure (Pa)
q = coefficient in the holdup correlation
RANS = Reynolds-Averaged Navier–Stokes
$Re_b = \rho_k|\mathbf{u}_j - \mathbf{u}_k|d_j/\mu_k$ Reynolds number
t = time (s)
T = temperature (°C)
$\mathbf{u}$ = velocity vector (m/s)
u_b = bubble velocity (m/s)
U_{swarm} = swarm bubble velocity (m/s)
U_{trans} = transition superficial velocity (m/s)
URANS = unsteady RANS
α = volume fraction
Δt = sampling period or time step size (s)
ε_G = gas holdup
$\varepsilon_{G,Local}$ = local void fraction
μ = dynamic viscosity (kg/(m s))
ρ = density (kg/m^3)
σ = surface tension coefficient (N/m)
$\bar{\tau}$ = viscous and Reynolds stresses ($kg/(m\ s^2)$)
φ = aspect ratio

References

[1] Brooks, C. S., Paranjape, S. S., Ozar, B., Hibiki, T., and Ishii, M., 2012, "Two-Group Drift-Flux Model for Closure of the Modified Two-Fluid Model," Int. J. Heat Fluid Flow, **37**, pp. 196–208.
[2] Shawkat, M. E., and Ching, C. Y., 2011, "Liquid Turbulence Kinetic Energy Budget of Co-Current Bubbly Flow in a Large Diameter Vertical Pipe," ASME J. Fluids Eng., **133**(9), p. 091303.
[3] Yamaguchi, K., and Yamazaki, Y., 1982, "Characteristics of Counter Current Gas–Liquid Two-Phase Flow in Vertical Tubes," J. Nucl. Sci. Technol., **19**(12), pp. 985–996.
[4] Hasan, A. R., Kabir, C. S., and Srinivasan, S., 1994, "Countercurrent Bubble and Slug Flows in a Vertical System," Chem. Eng. Sci., **49**(16), pp. 2567–2574.
[5] Aritomi, M., Zhou, S., Nakajima, M., Takeda, Y., Mori, M., and Yoshioka, Y., 1996, "Measurement System of Bubbly Flow Using Ultrasonic Velocity Profile Monitor and Video Data Processing Unit," J. Nucl. Sci. Technol., **33**(12), pp. 915–923.
[6] Fuangworawong, N., Kikura, H., Aritomi, M., and Komeno, T., 2007, "Tomographic Imaging of Counter-Current Bubbly Flow by Wire Mesh Tomography," Chem. Eng. J., **130**(2–3), pp. 111–118.
[7] Ghosh, S., Pratihar, D. K., Maiti, B., and Das, P. K., 2012, "Identification of Flow Regimes Using Conductivity Probe Signals and Neural Networks for Counter-Current Gas–Liquid Two-Phase Flow," Chem. Eng. Sci., **84**, pp. 417–436.
[8] Ghosh, S., Pratihar, D. K., Maiti, B., and Das, P. K., 2013, "Automatic Classification of Vertical Counter-Current Two-Phase Flow by Capturing Hydrodynamic Characteristics Through Objective Descriptions," Int. J. Multiphase Flow, **52**, pp. 102–120.
[9] Youssef Ahmed, A., Al-Dahhan Muthanna, H., and Dudukovic Milorad, P., 2013, "Bubble Columns With Internals: A Review," Int. J. Chem. React. Eng., **11**(1), pp. 169–223.
[10] Al-Oufi, F. M., Cumming, I. W., and Rielly, C. D., 2010, "Destabilisation of Homogeneous Bubbly Flow in an Annular Gap Bubble Column," Can. J. Chem. Eng., **88**(4), pp. 482–490.
[11] Julia, J. E., Ozar, B., Dixit, A., Jeong, J.-J., Hibiki, T., and Ishii, M., 2009, "Axial Development of Flow Regime in Adiabatic Upward Two-Phase Flow in a Vertical Annulus," ASME J. Fluids Eng., **131**(2), p. 021302.
[12] Das, G., Das, P. K., Purohit, N. K., and Mitra, A. K., 1999, "Flow Pattern Transition During Gas Liquid Upflow Through Vertical Concentric Annuli—Part I: Experimental Investigations," ASME J. Fluids Eng., **121**(4), pp. 895–901.
[13] Besagni, G., Guédon, G., and Inzoli, F., 2014, "Experimental Investigation of Counter Current Air–Water Flow in a Large Diameter Vertical Pipe With Inners," J. Phys.: Conf. Ser., **547**(1), p. 012024.
[14] Ziegenhein, T., Rzehak, R., and Lucas, D., 2015, "Transient Simulation for Large Scale Flow in Bubble Columns," Chem. Eng. Sci., **122**(27), pp. 1–13.
[15] Masood, R. M. A., and Delgado, A., 2014, "Numerical Investigation of the Interphase Forces and Turbulence Closure in 3D Square Bubble Columns," Chem. Eng. Sci., **108**, pp. 154–168.
[16] Laborde-Boutet, C., Larachi, F., Dromard, N., Delsart, O., and Schweich, D., 2009, "CFD Simulation of Bubble Column Flows: Investigations on Turbulence Models in RANS Approach," Chem. Eng. Sci., **64**(21), pp. 4399–4413.
[17] Masood, R. M. A., Khalid, Y., and Delgado, A., 2015, "Scale Adaptive Simulation of Bubble Column Flows," Chem. Eng. J., **262**, pp. 1126–1136.
[18] Masood, R. M. A., Rauh, C., and Delgado, A., 2014, "CFD Simulation of Bubble Column Flows: An Explicit Algebraic Reynolds Stress Model Approach," Int. J. Multiphase Flow, **66**, pp. 11–25.
[19] Zhang, D., Deen, N. G., and Kuipers, J. A. M., 2006, "Numerical Simulation of the Dynamic Flow Behavior in a Bubble Column: A Study of Closures for Turbulence and Interface Forces," Chem. Eng. Sci., **61**(23), pp. 7593–7608.

[20] Ziegenhein, T., Lucas, D., Rzehak, R., and Krepper, E., 2013, "Closure Relations for CFD Simulation of Bubble Columns," 8th International Conference on Multiphase Flow, ICMF 2013, Jeju, Korea, May 26–31, pp. 1–11.
[21] Pourtousi, M., Sahu, J. N., and Ganesan, P., 2014, "Effect of Interfacial Forces and Turbulence Models on Predicting Flow Pattern Inside the Bubble Column," Chem. Eng. Process., **75**, pp. 38–47.
[22] Tabib, M. V., Roy, S. A., and Joshi, J. B., 2008, "CFD Simulation of Bubble Column—An Analysis of Interphase Forces and Turbulence Models," Chem. Eng. J., **139**(3), pp. 589–614.
[23] Besagni, G., and Inzoli, F., 2015, "Role of Interfacial Forces in Bubble Column Simulations," 33rd UIT Heat Transfer Conference, L'Aquila, Italy, June 22–24.
[24] Reilly, I., Scott, D., Debruijn, T., and MacIntyre, D., 1994, "The Role of Gas Phase Momentum in Determining Gas Holdup and Hydrodynamic Flow Regimes in Bubble Column Operations," Can. J. Chem. Eng., **72**(1), pp. 3–12.
[25] Aloufi, F. M., 2011, "An Investigation of Gas Void Fraction and Transition Conditions for Two-Phase Flow in an Annular Gap Bubble Column," Ph.D. thesis, Loughborough University, Loughborough, UK.
[26] Honkanen, M., Saarenrinne, P., Stoor, T., and Niinimäki, J., 2005, "Recognition of Highly Overlapping Ellipse-Like Bubble Images," Meas. Sci. Technol., **16**(9), pp. 1760–1770.
[27] Lage, P. L. C., and Espósito, R. O., 1999, "Experimental Determination of Bubble Size Distributions in Bubble Columns: Prediction of Mean Bubble Diameter and Gas Hold Up," Powder Technol., **101**(2), pp. 142–150.
[28] Wongsuchoto, P., Charinpanitkul, T., and Pavasant, P., 2003, "Bubble Size Distribution and Gas–Liquid Mass Transfer in Airlift Contactors," Chem. Eng. J., **92**(1–3), pp. 81–90.
[29] Rakoczy, R., and Masiuk, S., 2009, "Experimental Study of Bubble Size Distribution in a Liquid Column Exposed to a Rotating Magnetic Field," Chem. Eng. Process., **48**(7), pp. 1229–1240.
[30] Hanselmann, W., and Windhab, E., 1998, "Flow Characteristics and Modelling of Foam Generation in a Continuous Rotor/Stator Mixer," J. Food Eng., **38**(4), pp. 393–405.
[31] Passos, A. D., Voulgaropoulos, V. P., Paras, S. V., and Mouza, A. A., 2015, "The Effect of Surfactant Addition on the Performance of a Bubble Column Containing a Non-Newtonian Liquid," Chem. Eng. Res. Des., **95**, pp. 93–104.
[32] Boes, R. M., and Hager, W. H., 1998, "Fiber-Optical Experimentation in Two-Phase Cascade Flow," International RCC Dams Seminar, K. Hansen, ed., Denver, pp. 1–13.
[33] Barrau, E., Rivière, N., Poupot, C., and Cartellier, A., 1999, "Single and Double Optical Probes in Air–Water Two-Phase Flows: Real Time Signal Processing and Sensor Performance," Int. J. Multiphase Flow, **25**(2), pp. 229–256.
[34] Simonnet, M., Gentric, C., Olmos, E., and Midoux, N., 2007, "Experimental Determination of the Drag Coefficient in a Swarm of Bubbles," Chem. Eng. Sci., **62**(3), pp. 858–866.
[35] Vejražka, J., Večeř, M., Orvalho, S., Sechet, P., Ruzicka, M. C., and Cartellier, A., 2010, "Measurement Accuracy of a Mono-Fiber Optical Probe in a Bubbly Flow," Int. J. Multiphase Flow, **36**(7), pp. 533–548.
[36] Zhang, W., and Zhu, D. Z., 2013, "Bubble Characteristics of Air–Water Bubbly Jets in Crossflow," Int. J. Multiphase Flow, **55**, pp. 156–171.
[37] Chang, K.-A., Lim, H.-J., and Su, C. B., 2003, "Fiber Optic Reflectometer for Velocity and Fraction Ratio Measurements in Multiphase Flows," Rev. Sci. Instrum., **74**(7), pp. 3559–3565.
[38] Lima Neto, I., Zhu, D., and Rajaratnam, N., 2008, "Air Injection in Water With Different Nozzles," J. Environ. Eng., **134**(4), pp. 283–294.
[39] Kiambi, S. L., Duquenne, A.-M., Dupont, J. B., Colin, C., Risso, F., and Delmas, H., 2003, "Measurements of Bubble Characteristics: Comparison Between Double Optical Probe and Imaging," Can. J. Chem. Eng., **81**(3–4), pp. 764–770.
[40] Chaumat, H., Billet-Duquenne, A. M., Augier, F., Mathieu, C., and Delmas, H., 2005, "Application of the Double Optic Probe Technique to Distorted Tumbling Bubbles in Aqueous or Organic Liquid," Chem. Eng. Sci., **60**(22), pp. 6134–6145.
[41] Cartellier, A., and Barrau, E., 1998, "Monofiber Optical Probes for Gas Detection and Gas Velocity Measurements: Conical Probes," Int. J. Multiphase Flow, **24**(8), pp. 1265–1294.
[42] Ishii, M., and Hibiki, T., 2011, *Thermo-Fluid Dynamics of Two-Phase Flow*, Springer-Verlag New York.
[43] Rzehak, R., and Krepper, E., 2013, "Closure Models for Turbulent Bubbly Flows: A CFD Study," Nucl. Eng. Des., **265**, pp. 701–711.
[44] Tomiyama, A., Tamai, H., Zun, I., and Hosokawa, S., 2002, "Transverse Migration of Single Bubbles in Simple Shear Flows," Chem. Eng. Sci., **57**(11), pp. 1849–1858.
[45] Wellek, R. M., Agrawal, A. K., and Skelland, A. H. P., 1966, "Shape of Liquid Drops Moving in Liquid Media," AIChE J., **12**(5), pp. 854–862.
[46] Burns, A. D., Frank, T., Hamill, I., and Shi, J.-M., 2004, "The Favre Averaged Drag Model for Turbulent Dispersion in Eulerian Multi-Phase Flows," 5th International Conference on Multiphase Flow, ICMF'04, Yokohama, Japan, May 30–June 4, pp. 1–17.
[47] Antal, S. P., Lahey, R. T., Jr., and Flaherty, J. E., 1991, "Analysis of Phase Distribution in Fully Developed Laminar Bubbly Two-Phase Flow," Int. J. Multiphase Flow, **17**(5), pp. 635–652.
[48] Besagni, G., Guédon, G., and Inzoli, F., 2014, "Experimental and Numerical Study of Counter-Current Flow in a Vertical Pipe," ASME Paper No. ESDA2014-20053.
[49] Shaikh, A., and Al-Dahhan, M. H., 2007, "A Review on Flow Regime Transition in Bubble Columns," Int. J. Chem. React. Eng., **5**(1), pp. 1–68.
[50] Krepper, E., Lucas, D., Frank, T., Prasser, H.-M., and Zwart, P. J., 2008, "The Inhomogeneous MUSIG Model for the Simulation of Polydispersed Flows," Nucl. Eng. Des., **238**(7), pp. 1690–1702.
[51] Lau, Y. M., Sujatha, K. T., Gaeini, M., Deen, N. G., and Kuipers, J. A. M., 2013, "Experimental Study of the Bubble Size Distribution in a Pseudo-2D Bubble Column," Chem. Eng. Sci., **98**, pp. 203–211.
[52] Hernandez-Aguilar, J. R., Coleman, R. G., Gomez, C. O., and Finch, J. A., 2004, "A Comparison Between Capillary and Imaging Techniques for Sizing Bubbles in Flotation Systems," Miner. Eng., **17**(1), pp. 53–61.
[53] Parthasarathy, R., and Ahmed, N., 1994, "Bubble Size Distribution in a Gas Sparged Vessel Agitated by a Rushton Turbine," Ind. Eng. Chem. Res., **33**(3), pp. 703–711.
[54] Kelessidis, V. C., and Dukler, A. E., 1989, "Modeling Flow Pattern Transitions for Upward Gas–Liquid Flow in Vertical Concentric and Eccentric Annuli," Int. J. Multiphase Flow, **15**(2), pp. 173–191.
[55] Otake, T., Tone, S., and Shinohara, K., 1981, "Gas Holdup in the Bubble Column With Cocurrent and Countercurrent Gas–Liquid Flow," J. Chem. Eng. Jpn., **14**(4), pp. 338–340.
[56] Akita, K., and Yoshida, F., 1973, "Gas Holdup and Volumetric Mass Transfer Coefficient in Bubble Columns: Effects of Liquid Properties," Ind. Eng. Chem. Process Des. Dev., **12**(1), pp. 76–80.
[57] Krishna, R., Wilkinson, P. M., and Van Dierendonck, L. L., 1991, "A Model for Gas Holdup in Bubble Columns Incorporating the Influence of Gas Density on Flow Regime Transitions," Chem. Eng. Sci., **46**(10), pp. 2491–2496.
[58] Schumpe, A., and Grund, G., 1986, "The Gas Disengagement Technique for Studying Gas Holdup Structure in Bubble Columns," Can. J. Chem. Eng., **64**(6), pp. 891–896.
[59] Wilkinson, P. M., Spek, A. P., and van Dierendonck, L. L., 1992, "Design Parameters Estimation for Scale-Up of High-Pressure Bubble Columns," AIChE J., **38**(4), pp. 544–554.
[60] Letzel, H. M., Schouten, J. C., Krishna, R., and van den Bleek, C. M., 1999, "Gas Holdup and Mass Transfer in Bubble Column Reactors Operated at Elevated Pressure," Chem. Eng. Sci., **54**(13–14), pp. 2237–2246.
[61] Ruzicka, M. C., Drahovs, J., Fialova, M., and Thomas, N. H., 2001, "Effect of Bubble Column Dimensions on Flow Regime Transition," Chem. Eng. Sci., **56**(21–22), pp. 6117–6124.
[62] Hur, Y. G., Yang, J. H., Jung, H., and Park, S. B., 2013, "Origin of Regime Transition to Turbulent Flow in Bubble Column: Orifice- and Column-Induced Transitions," Int. J. Multiphase Flow, **50**, pp. 89–97.
[63] Zahradnik, J., Fialova, M., Ruvzivc, M., Drahovs, J., Kavstanek, F., and Thomas, N. H., 1997, "Duality of the Gas–Liquid Flow Regimes in Bubble Column Reactors," Chem. Eng. Sci., **52**(21–22), pp. 3811–3826.
[64] Besagni, G., and Inzoli, F., 2015, "Influence of Electrolyte Concentration on Holdup, Flow Regime Transition and Local Flow Properties in a Large Scale Bubble Column," 33rd UIT Heat Transfer Conference, L'Aquila, Italy, June 22–24.
[65] Dargar, P., and Macchi, A., 2006, "Effect of Surface-Active Agents on the Phase Holdups of Three-Phase Fluidized Beds," Chem. Eng. Process., **45**(9), pp. 764–772.
[66] Rollbusch, P., Becker, M., Ludwig, M., Bieberle, A., Grünewald, M., Hampel, U., and Franke, R., 2015, "Experimental Investigation of the Influence of Column Scale, Gas Density and Liquid Properties on Gas Holdup in Bubble Columns," Int. J. Multiphase Flow, **75**, pp. 88–106.
[67] Reith, T., Renken, S., and Israel, B. A., 1968, "Gas Hold-Up and Axial Mixing in the Fluid Phase of Bubble Columns," Chem. Eng. Sci., **23**(6), pp. 619–629.
[68] Thorat, B. N., Shevade, A. V., Bhilegaonkar, K. N., Aglawe, R. H., Parasu Veera, U., Thakre, S. S., Pandit, A. B., Sawant, S. B., and Joshi, J. B., 1998, "Effect of Sparger Design and Height to Diameter Ratio on Fractional Gas Hold-Up in Bubble Columns," Chem. Eng. Res. Des., **76**(7), pp. 823–834.
[69] Reilly, I. G., Scott, D. S., De Bruijn, T., Jain, A., and Piskorz, J., 1986, "A Correlation for Gas Holdup in Turbulent Coalescing Bubble Columns," Can. J. Chem. Eng., **64**(5), pp. 705–717.
[70] Joshi, J. B., and Sharma, M. M., 1979, "A Circulation Cell Model for Bubble Column," Trans. I. Chem. Eng., **57**, pp. 244–251.
[71] Hughmark, G. A., 1967, "Holdup and Mass Transfer in Bubble Columns," Ind. Eng. Chem. Process Des. Dev., **6**(2), pp. 218–220.
[72] Kawase, Y., and Moo-Young, M., 1987, "Theoretical Prediction of Gas Hold-Up in Bubble Columns With Newtonian and Non-Newtonian Fluids," Ind. Eng. Chem. Res., **26**(5), pp. 933–937.
[73] Hoang, N. H., Euh, D. J., Yun, B. J., and Song, C. H., 2015, "A New Method of Relating a Chord Length Distribution to a Bubble Size Distribution for Vertical Bubbly Flows," Int. J. Multiphase Flow, **71**, pp. 23–31.